ACS NANO

www.acsnano.org

ARTICLE

Lightweight Calcium–Silicate–Hydrate Nacre with High Strength and High Toughness

Yuhuan Wang, Yi Bao, and Weina Meng*

Cite This: *ACS Nano* 2024, 18, 23655–23671

Read Online

ACCESS | Metrics & More | Article Recommendations | Supporting Information

ABSTRACT: **Low flexural strength and toughness have posed enduring challenges to cementitious materials. As the main hydration product of cement, calcium silicate hydrate (C−S−H) plays important roles in the mechanical performance of cementitious materials while exhibiting random microstructures with pores and defects, which hinder mechanical enhancement. Inspired by the "brick-and-mortar" microstructure of natural nacre, this paper presents a method combining freeze casting, freeze-drying, in situ polymerization, and hot pressing to fabricate C−S−H nacre with high flexural strength, high toughness, and lightweight. Poly(acrylamide-*co*-acrylic acid) was used to disperse C−S−H and toughen C−S−H building blocks, which function as "bricks", while poly(methyl methacrylate) was impregnated as "mortar". The flexural strength, toughness, and density of C−S−H nacre reached 124 MPa, 5173 kJ/m^3, and 0.98 g/cm^3, respectively. The flexural strength and toughness of the C−S−H nacre are 18 and 1230 times higher than those of cement paste, respectively, with a 60% reduction in density, outperforming existing cementitious materials and natural nacre. This research establishes the relationship between material composition, fabrication process, microstructure, and mechanical performance, facilitating the design of high-performance C−S−H-based and cement-based composites for scalable engineering applications.**

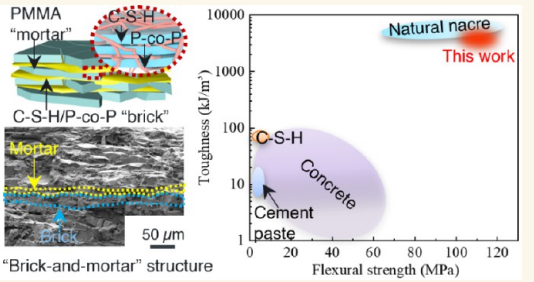

KEYWORDS: *"brick-and-mortar" hierarchical microstructure, calcium silicate hydrate (C−S−H), C−S−H nacre, C−S−H/polymer composite, flexural performance, lightweight*

INTRODUCTION

Concrete is the most widely used construction material worldwide. The annual consumption of concrete was 10 billion tons in 2020.[1] Compared with other construction materials, such as steel and wood, concrete features advantages such as wide availability, high fire resistance, low material cost, and high compressive strength. However, concrete is weak and brittle in tension.[2,3] The low tensile properties have caused major issues in various civil structures, such as bridges, buildings, and roads, which are usually subjected to flexural loads that cause tensile stresses in concrete. A predominant concern arising from these stresses is cracking. Such cracks can originate from various factors including mechanical loads,[4,5] temperature changes,[6,7] and volume shrinkage of concrete.[8,9]

Traditional solutions for enhancing the mechanical properties of concrete have predominantly relied on using reinforcing bars, meshes, fibers, and so on.[10,11] Reinforcing bars and meshes have been embedded in concrete to enhance tensile and flexural strengths, and chopped fibers have been dispersed in concrete to produce fiber-reinforced concrete.[8,9] While the above solutions effectively elevate the overall mechanical properties of concrete, such as improving the flexural strengths of beams[12] and slabs,[13,14] they failed to significantly enhance the intrinsic mechanical properties of concrete matrix.

An emerging solution garnering significant attention involves strengthening the mechanical properties of concrete matrix by using nanomaterials, such as carbon nanofibers and various types of nanoparticles.[15,16] Nanomaterials help densify the microstructures of concrete matrix by promoting cement hydration and filling micropores.[17,18] For example, the flexural strength of concrete increased from 7.7 to 11.3 MPa, a 46% improvement, via adding 0.3% carbon nanofibers.[19] Despite the notable improvement, the flexural strength of concrete remains low. In general, the flexural strength of concrete is lower than 30 MPa.[20−22] An important reason is the highly disordered hydration products and pore structures.

Calcium silicate hydrate (C−S−H) is the predominant hydration product of cement, making up over 60% of the total

Received: June 19, 2024
Revised: August 6, 2024
Accepted: August 7, 2024
Published: August 14, 2024

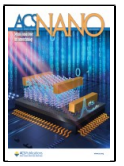

https://doi.org/10.1021/acsnano.4c08200
ACS Nano 2024, 18, 23655−23671

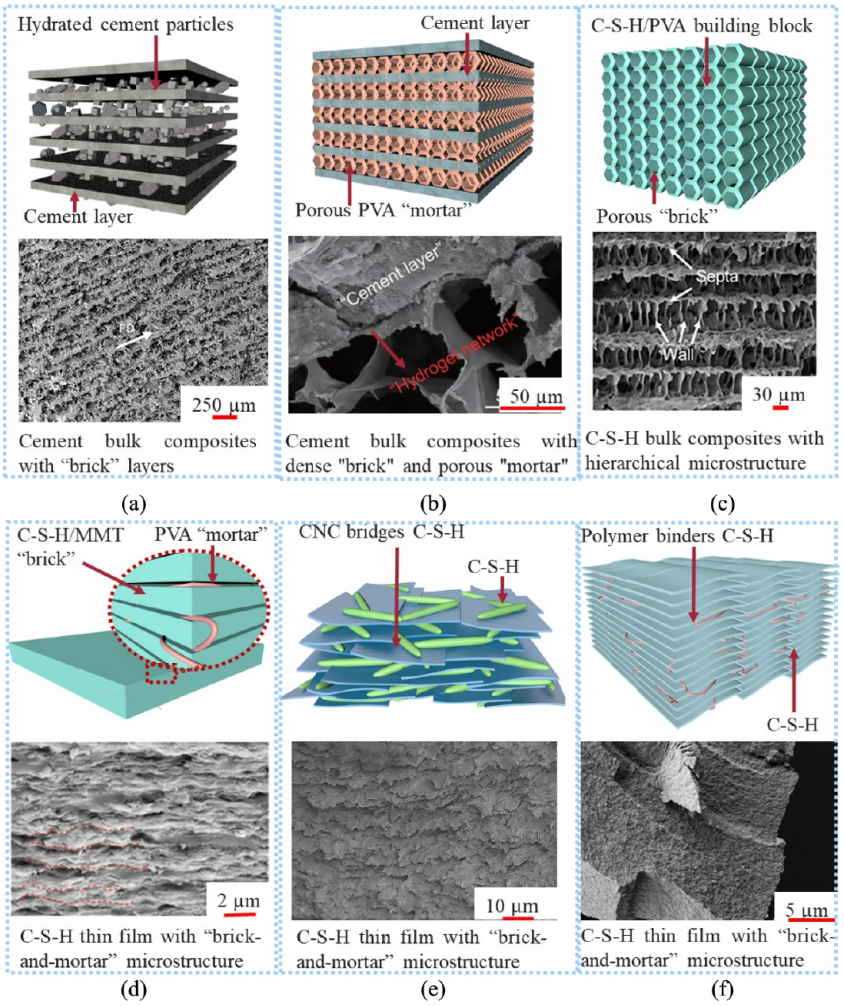

Figure 1. Nacre inspired materials: (a) cement bulk composite with hierarchical "brick" layers,[52] (b) cement bulk composite with dense "brick" and porous PVA "mortar",[53] (c) C−S−H bulk composites with hierarchical microstructure,[35] (d) PVA and MMT regulated C−S−H thin film,[54] (e) CNC regulated C−S−H thin film,[55] and (f) polymer regulated C−S−H mesocrystal.[25]

hydration products by volume.[23] C−S−H stands as the main binder, underpinning mechanical properties, shrinkage, and durability of cementitious materials.[23,24] As a result, C−S−H is recognized as the foundation of cementitious materials, yet it displays gel-like amorphous microstructures with distributed defects (i.e., poor crystalline).[25−27] The inherent random microstructure of C−S−H leads to concrete cracking, as fractures tend to originate from the weakest points and subsequently propagate along the vulnerable path within the disordered microstructure. Therefore, refining and regulating the microstructure of C−S−H presents an enticing avenue to intrinsically enhance the concrete matrix.

Manipulation of the C−S−H composition, microstructure, and properties has gained considerable interest in recent years. This is because C−S−H has substantial impact on not only cementitious materials but also other fields, such as bone tissue engineering,[28] drug delivery,[29] wastewater treatment,[30−33] energy storage,[34] and thermal insulation.[35,36] One of the most effective ways to enhance the mechanical performance of C−S−H is to refine its microstructures through improving structural order and eliminating pores and defects.[27,37]

Graphene oxide was used to reinforce C−S−H, resulting in a 52.6% increase in Young's modulus and a 23.3% increase in tensile strength, according to molecular dynamic simulation.[38] The enhancement arose from high interfacial interaction energy and physical interlocking between GO and C−S−H, facilitating efficient load transfer.[38] Molecular dynamic analysis confirmed that an increase in the aspect ratio (diameter to thickness ratio) of C−S−H resulted in the encapsulation of larger-sized pores, consequently resulting in reduced modulus and hardness.[39] Liu et al.[40] studied how cellulose fibers interacted with C−S−H and confirmed that electrostatic and hydrogen bonds increased the adhesion between C−S−H and cellulose fibers, thus improving the mechanical performance of cementitious materials. Most previous research on modifying C−S−H relied on simulations at the molecular and nanoscale levels. To implement the theoretical concepts and results in real-world applications, it is essential to develop experimental and scalable fabrication methods that can be smoothly integrated into macroscopic structures.

Natural nacre, commonly known as "mother of pearl", has been researched over three decades for its exceptional mechanical properties over multiple length scales.[41] Nacre shows low density, high strength, high toughness, and excellent crack tolerance due to its unique "brick-and-mortar" hierarchical microstructure. Rigid yet brittle aragonite functions as the "brick" for providing mechanical strengths, while soft yet ductile organic polymers function as the "mortar"

https://doi.org/10.1021/acsnano.4c08200
ACS Nano 2024, 18, 23655−23671

for providing toughness.[42] The main toughening mechanisms include the viscoelastic deformation of the "mortar" layers and the subsequent "pull-out" of mineral "bricks".[43] Additional factors contributing to its toughness include resistance from nanoasperities, mineral bridges, and platelet interlocking.

Numerous nacre-inspired cementitious materials have been fabricated by mimicking the hierarchical architecture of natural nacre.[44−51] For example, a cementitious composite with an oriented hierarchical microstructure, as shown in Figure 1a, was prepared via the ice-template method, yielding a compressive strength of 35 MPa.[52] Similarly, Chen et al.[53] fabricated a multilayered cementitious composite by incorporating poly(vinyl alcohol) (PVA) into cement paste, with the cement functioning as the "brick" and PVA functioning as the "mortar", as shown in Figure 1b. Such a layered microstructure increased the flexural strength from 2.65 MPa (plain cement paste) to 5.5 MPa. Although the cementitious composite showed a "brick-and-mortar" microstructure, its flexural strength was limited to 5.5 MPa due to two primary factors. First, in the "brick" layer, the presence of pores and the random orientation of C−S−H limited the mechanical improvement. Second, in the "mortar" layer, pores were also observed due to the high molecular weight and viscosity of PVA, making it difficult for PVA to penetrate into the interlayers.[53] In another research, a C−S−H-based composite with a hierarchical microstructure was fabricated via the ice-template method, demonstrating a tensile strength of 8.7 MPa and a tensile strain of 0.5 mm.[35] Although C−S−H was organized in a hierarchical microstructure, there were interlayer gaps between adjacent C−S−H-based "brick" layers, leading to limited mechanical properties, as shown in Figure 1c.[35,36] Additionally, a few studies have adopted nacre-inspired methods to enhance the mechanical strength and impact resistance. These methods include the addition of polymer membranes,[46,51] the incorporation of polymeric mesh,[46,47] and the weaving of steel mesh[45] between cementitious layers. However, most of the current nacre-inspired cementitious materials demonstrate a trade-off between flexural strength and toughness, and limited enhancements in flexural strength (below 60 MPa) and toughness (below 1470 kJ/m^3).[44−51,53]

To overcome the trade-off between flexural strength and toughness, dense "brick-and-mortar" microstructures have been achieved, resulting in superior mechanical performance. For example, Liu et al.[54] prepared a C−S−H-based thin film with a dense "brick-and-mortar" microstructure via vacuum filtration, as shown in Figure 1d. The composite used exfoliated montmorillonite (MMT)/C−S−H as the "brick" and PVA as the "mortar", leading to a tensile strength of 15.8 MPa and a toughness of 16 200 kJ/m^3.

Wang et al.[55] produced a C−S−H-based thin film with a "brick-and-mortar" microstructure via vacuum filtration of C−S−H and cellulose nanocrystals (CNC), as shown in Figure 1e. CNC functioned as both bridges and binders linking adjacent C−S−H layers, resulting in the C−S−H/CNC nanocomposite achieving a flexural strength of 83 MPa and a toughness of 3867 kJ/m^3. Following a similar process, Picker et al.[25] fabricated highly ordered C−S−H mesocrystals by aligning C−S−H nanoplatelets and binding them with a polymer, as shown in Figure 1f. The resulting thin C−S−H-based film achieved a flexural strength up to 153 MPa. De Souza et al.[27] and Starr et al.[56] fabricated thin films using C−S−H/GO and C−S−H/styrene−butadiene composites, respectively, with dense "brick-and-mortar" microstructures, simultaneously achieving high mechanical strengths and toughness. Various dense "brick-and-mortar" microstructures have been developed, all demonstrating mechanical improvements. However, these advancements largely depend on the vacuum filtration of suspension, which restricts the size of the composites to thin films.

Despite the achievement of hierarchical microstructures of cement-based and C−S−H-based materials, three significant limitations have been identified:

- Limited mechanical performance: the mechanical strengths of cement-based and C−S−H-based materials were limited. For example, the flexural strength of the cement-based composite in reference[53] was 5.5 MPa, and the tensile strengths of C−S−H-based composites in references[35] and[54] were 8.7 and 15.8 MPa, respectively, insufficient for many applications, such as bridges and buildings requiring high mechanical strengths.
- Trade-off between mechanical strengths and toughness: Increasing the flexural strength often reduces toughness, and increasing toughness often reduces flexural strength. A few studies presented materials with high mechanical strengths and high toughness, but the fabrication methods were limited to thin films[25,54,56] and small samples.[55] It was unknown how to develop cementitious composites with high mechanical strengths and toughness while having up-scalability.
- Fabrication of "brick-and-mortar" hierarchical microstructures: Although prior research revealed that "brick-and-mortar" hierarchical microstructures have benefits of enhanced mechanical strength and toughness,[57−59] it was unclear how cement-based or C−S−H-based materials can achieve "brick-and-mortar" microstructures. C−S−H thin films were created through vacuum filtration, but the thicknesses of "brick" and "mortar" were not controlled, and the method for fabricating thin films were inapplicable for large-scale structural applications.

In short, developing high-performance C−S−H-based composites remains challenging due to the lack of a strategy that effectively balances flexural strength and toughness while achieving scalability, necessitating further investigation into toughening mechanisms.

The goal of this research is to develop a C−S−H composite by mimicking the structure of natural nacre. To this end, there are two primary objectives: (1) to develop a scalable approach to fabricate cementitious materials with dense "brick-and-mortar" microstructures and (2) to achieve high flexural strength and high toughness simultaneously. A fabrication method integrating freeze casting, freeze-drying, in situ polymerization, and hot pressing is presented to fabricate C−S−H-based composites with dense "brick-to-mortar" microstructures. The unique hierarchical microstructure allows C−S−H composites to arrest and bridge cracks, thereby impeding crack propagation. Moreover, poly(acrylamide-*co*-acrylic acid) is utilized to toughen C−S−H building blocks, which serve as the "bricks" to provide strength, while poly(methyl methacrylate) serves as "mortar" layers to provide toughness. Furthermore, mineral bridges, nanoasperities, and distinctive interlayer waviness were incorporated into the composites to deflect and arrest cracks as well as to dissipate fracture energy. The structural design and engineering

https://doi.org/10.1021/acsnano.4c08200
ACS Nano 2024, 18, 23655−23671

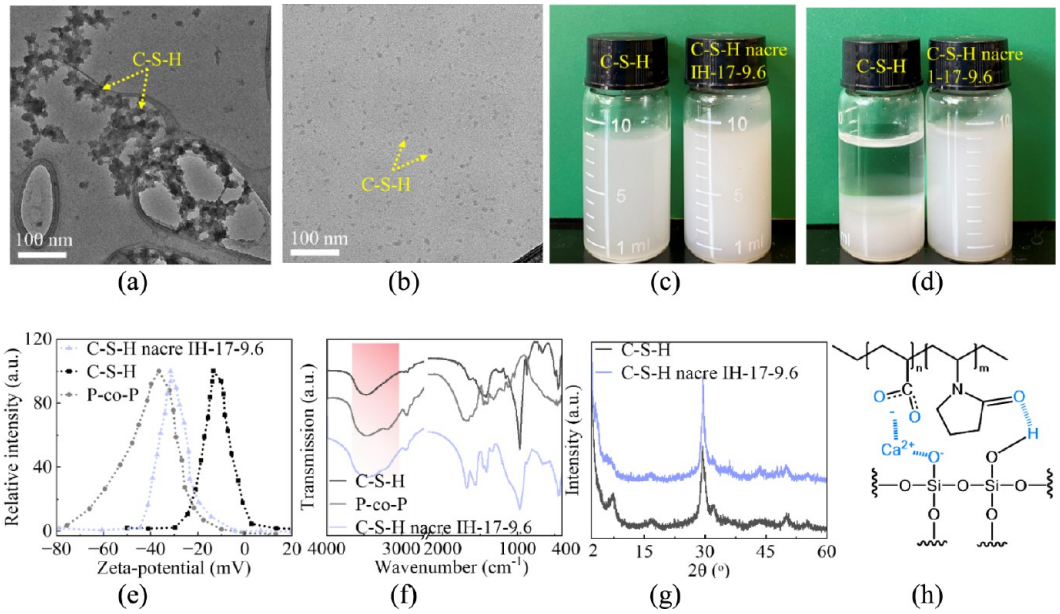

Figure 2. Stability of C−S−H building block suspensions: (a) visual observation at 5 min, (b) visual observation at 12 h, (c) TEM image of C−S−H without P-*co*-P, (d) TEM image of C−S−H with *p*-*co*-P, (e) zeta potential, (f) FTIR, (g) XRD, and (h) interaction between C−S−H and P-*co*-P.

techniques of C−S−H composites offer innovative pathways for enhancing both the strength and toughness of cementitious materials, enabling the fabrication of advanced construction materials.

RESULTS AND DISCUSSION

C−S−H Building Blocks. The stability characterizations of pure C−S−H and C−S−H building blocks are shown in Figure 2. Photos of C−S−H and C−S−H nacre IH-17-9.6 suspensions are shown in Figure 2a,b. Without using P-*co*-P, C−S−H tended to aggregate and precipitate rapidly due to prominent secondary nucleation and attractive forces between C−S−H nanoparticles.[60] In the presence of P-*co*-P, the C−S−H building blocks achieved the desired colloidal stability and even dispersion.

The TEM images showed the morphologies of C−S−H and C−S−H building blocks in Figures 2c,d. The diameters of C−S−H aggregates were 200 nm to 1000 nm, and the diameters of C−S−H nanoparticles were 20 to 40 nm, confirming that P-*co*-P can hinder the agglomeration of C−S−H. The mechanism is that the hydroxy and carboxylic functional groups of P-*co*-P interact with the hydroxyl groups of C−S−H via calcium ion coordination bonds and hydrogen bonds,[55] thus hindering the secondary nucleation of C−S−H nanoparticles.

Furthermore, the effect of P-*co*-P on the stability of C−S−H suspension was investigated using the measurement of the zeta potential, as shown in Figure 2e. According to reference[61], a suspension is stable when its absolute value of zeta potential exceeds 30 mV. In the absence of P-*co*-P, the absolute values of zeta potential were smaller than 30 mV; however, in the presence of P-*co*-P, the absolute values of zeta potential were larger than 30 mV, indicating that P-*co*-P is effective in hindering the agglomeration of C−S−H. The reason is that P-*co*-P can absorb at the solid−liquid interface between C−S−H and aqueous phase via the carboxylate groups. The adsorption facilitates steric hindrance, effectively preventing the agglomeration of C−S−H nanoparticles.[62]

To verify the interfacial interactions between P-*co*-P and C−S−H, FTIR measurements were performed, as shown in Figure 2f. With the addition of P-*co*-P, the hydroxyl peak at 3450 cm^{-1} was broadened and shifted toward lower wavenumbers, indicating the formation of hydrogen bonds and calcium ion coordination bonds between C−S−H and P-*co*-P.[55,63] The broadened H−O−H bending vibrations at 1660 cm^{-1} confirmed the formation of hydrogen bonds.[55,64] XRD spectra are provided, as shown in Figure 2g. The XRD spectra of the C−S−H nacre IH-17-9.6 were similar to the XRD spectra of pure C−S−H. There was no new diffraction peak, indicating that the addition of P-*co*-P did not change the crystalline structure of C−S−H. The interfacial interactions between C−S−H and P-*co*-P via calcium ion coordination bonds and hydrogen bonds are shown in Figure 2h.

The SEM images of the cross section of porous lamellar structures are shown in Figure 3a−d. The samples had the same C−S−H to P-to-P ratio but different C−S−H solid contents. All porous lamellar structures exhibited a long-range aligned architecture, but they exhibited different wall density. The illustration of wall density is shown in Figure 3e. As the C−S−H solid content increased, the wall density increased from around 8 to 54 wall/mm, and bridges appeared to connect the adjacent layers (Figure 3c,d). The increase in C−S−H solid content increased the volume of C−S−H nanoparticles being trapped within the ice crystals. Consequently, an increased number of mineral bridges formed between the adjacent layers, which is an important factor in enhancing the mechanical properties of nacre-mimicking composites.[65]

Another important finding is that C−S−H nacre IH-0-9.6, fabricated using the same way as C−S−H nacre IH-17-9.6, collapsed after performing the freeze-drying operation, which was also reported in other studies.[36,54] The collapse is attributed to the absence of P-*co*-P, which serves as the binder phase to entangle the C−S−H nanoparticles together and preserve the layered scaffold. The microstructure of C−S−H-36-9.6-d is shown in Figure S2. A photo of the C−S−H porous

https://doi.org/10.1021/acsnano.4c08200
ACS Nano 2024, 18, 23655−23671

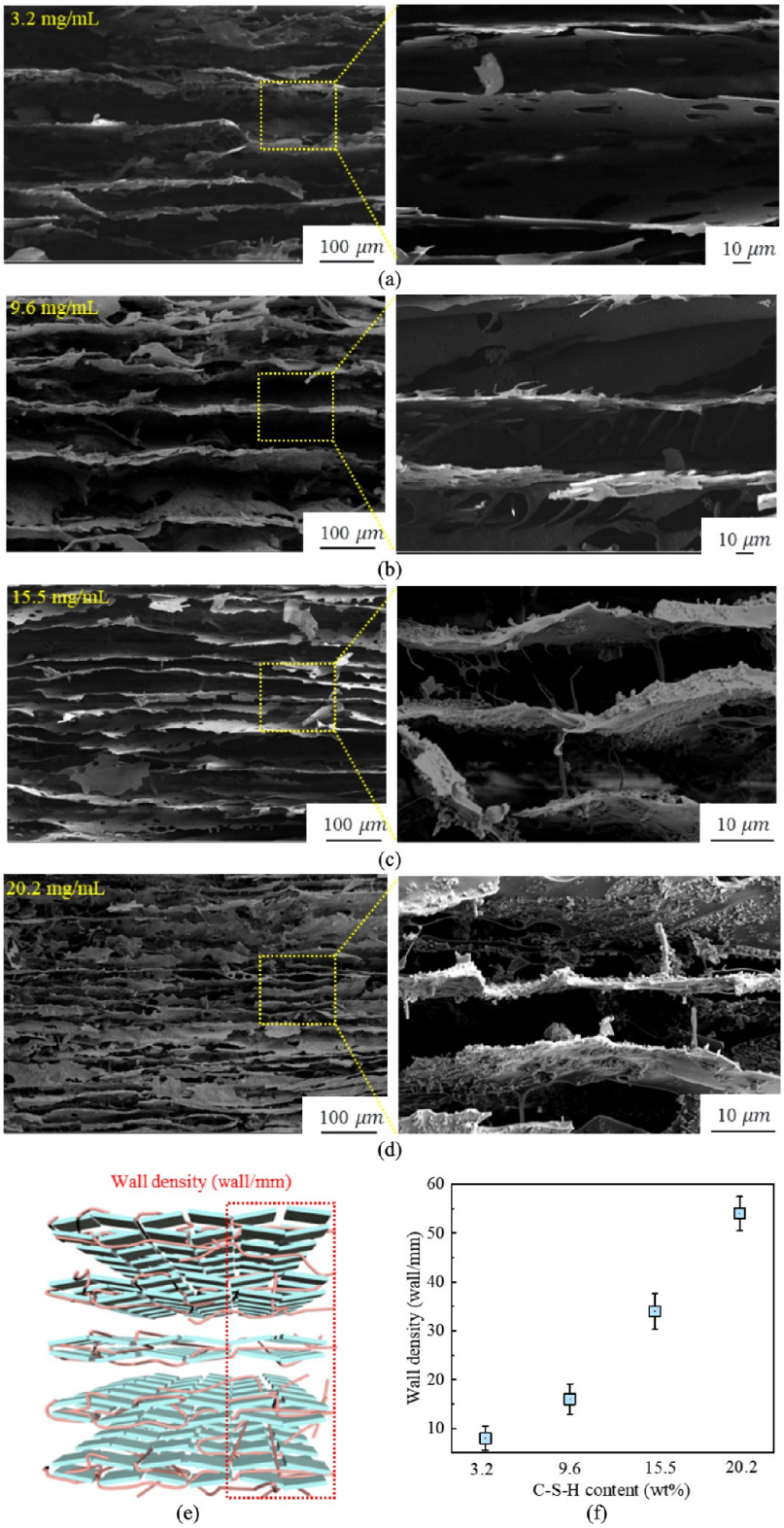

Figure 3. SEM images and characteristics of the porous lamellar structure: (a) C−S−H nacre IH-36-3.2, (b) C−S−H nacre IH-36-9.6, (c) C−S−H nacre IH-36-15.5, and (d) C−S−H nacre IH-36-20.2. (e) Illustration of wall density and (f) statistical plot of wall density.

lamellar structure is shown in Figure S3. The dimensions of the C−S−H porous lamellar structure reached 100 mm, revealing the scalability of the methods.

C−S−H Nacre IH. The SEM images of the cross sections of C−S−H nacre IH samples with different C−S−H solid contents are shown in Figure 4a−d. The oriented lamellar structure was preserved after hot pressing. The single-layer thickness increased from 2 to 5 μm as the C−S−H content increased from 3 to 20 mg/mL (Figure 4e). The single-layer thickness has impact on both the size and quantity of flaws in the lamellar phase.[66] With the increase in the C−S−H solid content, bridges and waviness between C−S−H layers were

https://doi.org/10.1021/acsnano.4c08200
ACS Nano 2024, 18, 23655−23671

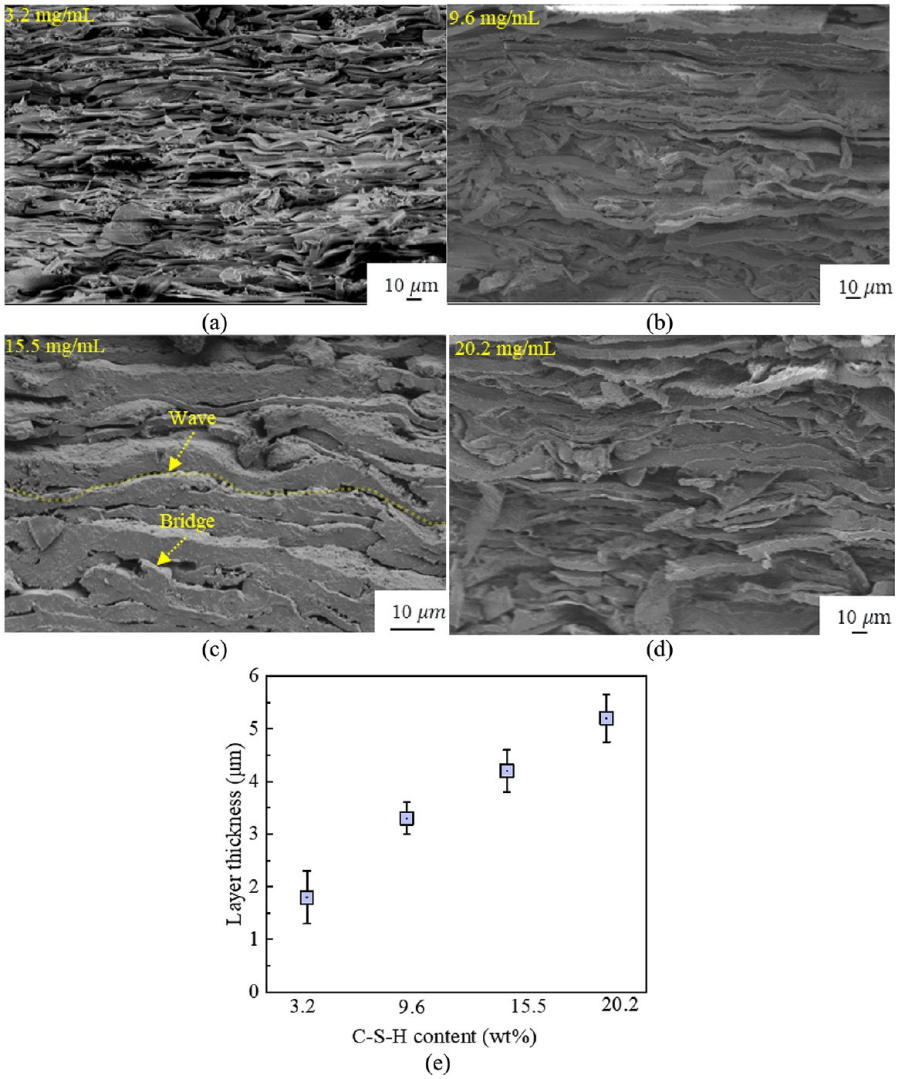

Figure 4. SEM images of C−S−H nacre IH: (a) C−S−H nacre IH-36-3.2, (b) C−S−H nacre IH-36-9.6, (c) C−S−H nacre IH-36-15.5, and (d) C−S−H nacre IH-36-20.2. (e) Layer thickness.

generated, as shown in Figure 4c. Similar mineral bridges and waviness were observed in natural nacres,[67] and it is believed that the presence of bridges and waviness introduces an effective mechanism for energy dissipation, thereby improving the toughness of nacre under mechanical loads.

C−S−H Nacre IPH. The SEM images of the cross section of the C−S−H nacre IPH with different PMMA layer thicknesses are shown in Figure 5. All C−S−H nacre IPH samples exhibited dense "brick-and-mortar" microstructures. The P-*co*-P toughened C−S−H was seen as packed "bricks" (shown in aqua), and the layers of "bricks" were separated by PMMA, which functioned as "mortar" (shown in yellow). C−S−H nacre IPH samples were prepared from the C−S−H nacre IH-36-15.5 porous lamellar structure with the "brick" thickness of 4 μm. The thickness of "mortar" was in the range of 1 to 5 μm. The TGA results confirmed that the PMMA content could be controlled via adjusting the lamellar spacing distance (Figure S5). The C−S−H nacre IPH exhibited mineral bridges, waviness, and asperities, which were characteristic features found in natural nacre.[67] Moreover, Figure S6 showcases the top surface and cross-section of C−S−H nacre IPH-36-15.5-2, highlighting the presence of asperities.

The energy dispersive spectrum mapping results provided detailed insights into the spatial distribution of "brick" and "mortar" layers, as shown in Figure S7. The mapping results highlighted carbon (C) and oxygen (O) distributions, revealing the arrangement of PMMA that forms "mortar" layers. The presence of calcium (Ca) and silicon (Si), which are key constituents of C−S−H, indicated "brick" layers. P-*co*-P, which also contained C and O, was observed in "brick" layers. The lower magnification SEM image in Figure S8 demonstrated the "brick-and-mortar" microstructure has been maintained after hot-pressing. The micro-CT analysis further verified the highly organized inner microstructure of C−S−H nacre IPH, as illustrated in Figure S9.

Flexural Properties. The results of flexural stress−strain curves; flexural strength; ultimate strain; and toughness of cement, C−S−H-36-9.6-d, C−S−H nacre IH, and C−S−H nacre IPH are shown in Figure 6 and Table S1. Based on the characteristics of microstructure and components, the dominating factors for enhancing the mechanical performance of C−S−H nacre are related to (1) P-*co*-P, (2) hierarchical microstructure, and (3) PMMA. The flexural properties of

https://doi.org/10.1021/acsnano.4c08200
ACS Nano 2024, 18, 23655−23671

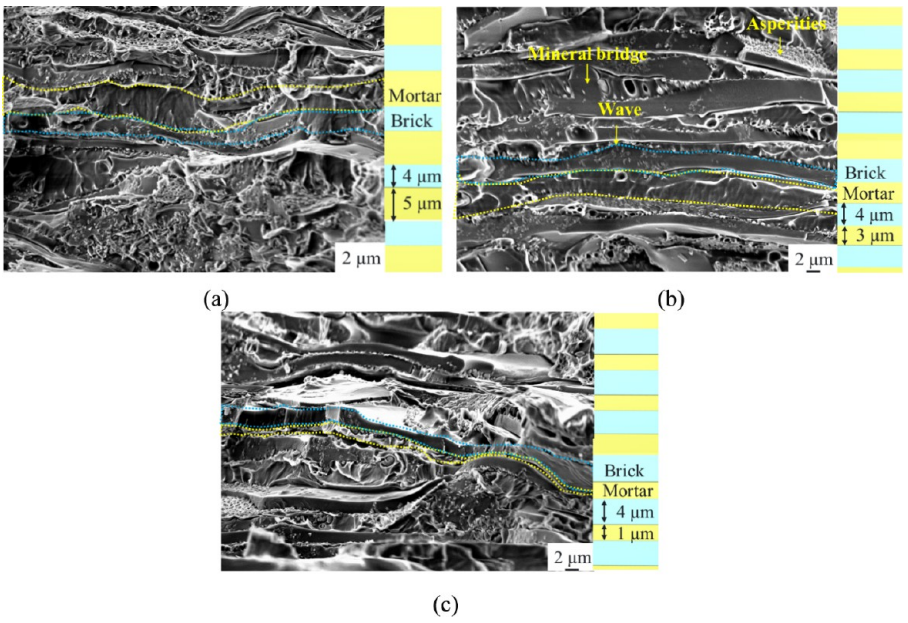

Figure 5. SEM images and illustration of C−S−H nacre IPH: (a) C−S−H nacre IPH-36-15.5-3, (b) C−S−H nacre IPH-36-15.5-2, and (c) C−S−H nacre IPH-36-15.5-1.

cement, C−S−H-36-9.6-d, C−S−H nacre IH, and C−S−H nacre IPH are discussed according to these categories:

Roles of P-co-P. P-*co*-P was used to toughen C−S−H via two mechanisms. First, it enhanced the dispersion of C−S−H in the suspension. Second, P-*co*-P absorbed onto the surface of C−S−H, toughening it to its hardened state. As shown in Figure 6a, the flexural strength, flexural strain, and toughness of cement were 7 MPa, 0.034%, and 4.2 kJ/m^3, respectively. In comparison, the flexural strength, flexural strain, and toughness of C−S−H-36-9.6-d were 8 MPa, 1.35%, and 71.1 kJ/m^3, respectively. The ultimate strain and toughness of C−S−H-36-9.6-d were significantly improved.

As shown Figure 6b, with the C−S−H content at 9.6 wt % and the increase of P-*co*-P content increased from 17 to 40 wt %, flexural strength initially increased from 22 to 41 MPa and then decreased to 39 MPa. Similarly, flexural strain increased from 1.36% to 1.95% and then decreased to 1.80%. Toughness also saw an initial increase from 71.1 to 385.6 kJ/m^3 before decreasing to 307.2 kJ/m^3. The highest mechanical performance of C−S−H nacre IH was achieved when the P-*co*-P content was 36 wt %. This is because P-*co*-P not only toughens C−S−H but also provides space for C−S−H layers to slip, effectively dissipating energy.[55,68] However, when the P-*co*-P content reached 40 wt %, the excess P-*co*-P may hinder the stress transfer between adjacent C−S−H layers.

Roles of Hierarchical Microstructures with Mineral Bridges, Asperities, and Waviness. The P-*co*-P toughened C−S−H functions as "bricks" to form hierarchical microstructures. The hierarchical microstructure could strengthen the composites and inhibit crack propagation. For example, C−S−H-36-9.6-d showed flexural strength, flexural strain, and toughness of 8 MPa, 1.35%, and 71.1 kJ/m^3, respectively. C−S−H nacre IH-36-9.6 showed 41 MPa in flexural strength, 1.95% in flexural strain, and 385.6 kJ/m^3 in toughness, respectively. The key distinction between C−S−H-36-9.6-d and C−S−H nacre IH-36-9.6 was that the latter material had a highly ordered hierarchical microstructure, highlighting the significant role of hierarchical microstructures in the mechanical performance of C−S−H nacre.

The thickness of the "brick" layers, along with the inclusion of mineral bridges, asperities, and waviness, further enhances the reinforcement of the composites. As the C−S−H content increased from 3.2 to 20.2 wt %, while keeping the *p*-*co*-P content at 36 wt %, the flexural strength initially increased from 39 to 53 MPa, then decreased to 46 MPa, as shown in Figure 6d. Similarly, the ultimate strain increased from 1.8% to 2.2% and then decreased to 2.1%, as shown in Figure 6e. The toughness also increased from 267.2 to 515.5 kJ/m^3 and then decreased to 443.8 kJ/m^3, as shown in Figure 6f. The optimal mechanical performance of C−S−H nacre IH was observed at a C−S−H content of 15.5 wt %. The increase in C−S−H content leads to interlayer bridges and asperities, which could prevent cracks and restrict crack propagation (Figure 4). Besides, wall thickness plays an important role since it affects the size and number of flaws in the single layer. C−S−H nacre IH with thicker walls exhibited increased resistance to stress, leading to improved flexural strength and flexural strain. However, as the wall thickness further increases, there is a bigger chance of encountering large pores within the single layer,[66] which explains the observed reduction in flexural strength and flexural strain.

Roles of PMMA. PMMA between "brick" layers functions as "mortar," which can arrest and bridge cracks, enhancing the toughness of the matrix. As illustrated in Figure 6c, C−S−H nacre IPH, with P-*co*-P toughened C−S−H as "brick" and "PMMA" as "mortar", carried higher loads than C−S−H nacre IH after peak loads. This improved performance is attributed to the "brick-and-mortar" microstructure of C−S−H nacre IPH. The P-*co*-P toughened C−S−H "brick" provides mechanical strength, and the PMMA "mortar" provides interface to arrest and deflect cracks, enhancing fracture toughness.[69] Under mechanical loads, the presence of nanoscale or microscale cracks in the material did not result in an abrupt fracture. Instead, the crack could be either arrested by the "mortar" (PMMA layer) or guided to propagate

https://doi.org/10.1021/acsnano.4c08200
ACS Nano 2024, 18, 23655−23671

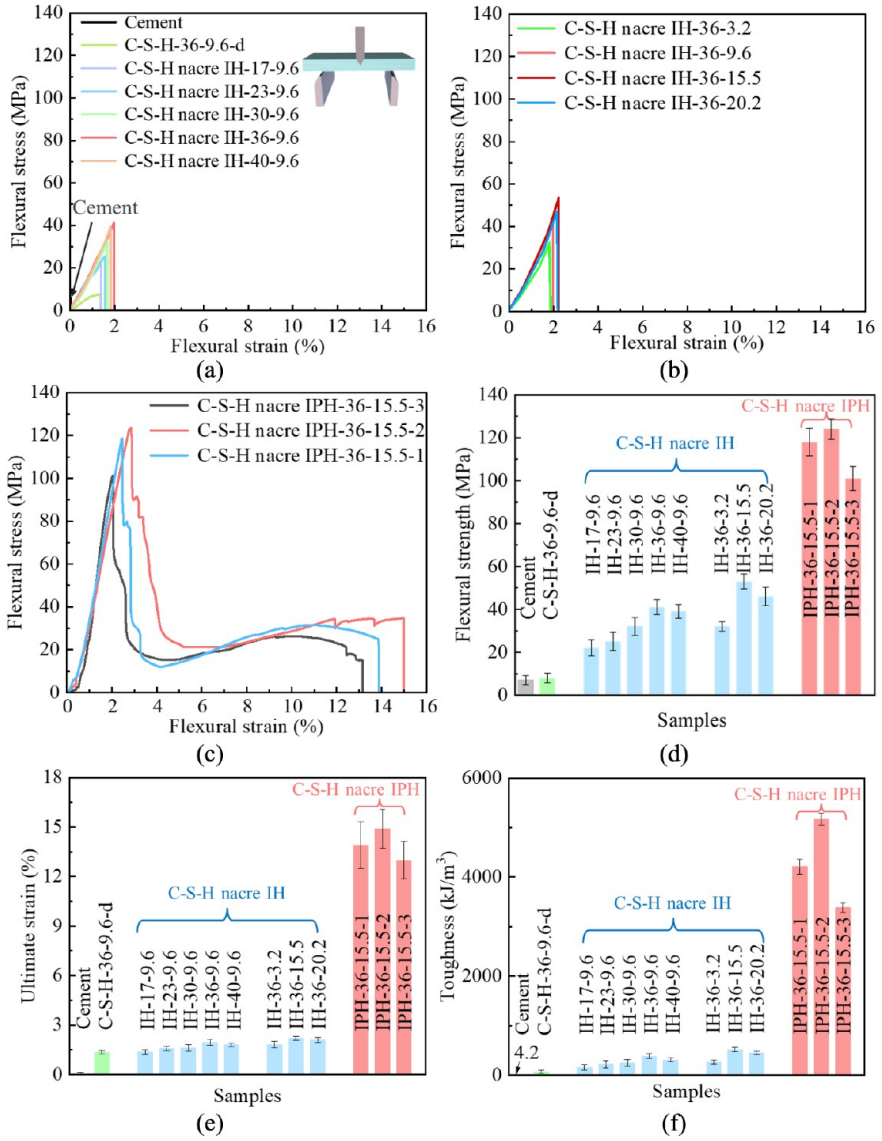

Figure 6. Flexural properties: flexural stress−strain curves of (a) C−S−H nacre IH under different P-*co*-P contents, (b) nacre IH under different C−S−H contents, (c) C−S−H nacre IPH, and statistic plots for (d) flexural strength, (e) ultimate strain, and (f) toughness.

along the "brick-to-mortar" interface with waviness, therefore effectively preventing cracks from propagating through the specimen and causing abrupt failure, significantly increasing the mechanical strength and toughness. This resilience is the underlying mechanism for the plateau in the curve, reflecting the C−S−H nacre's ability to maintain structural integrity under stress due to its unique microstructural characteristics.

The thickness of the PMMA "mortar" layers plays a critical role in enhancing the mechanical performance of the composites. While maintaining the P-*co*-P and C−S−H contents at 36 and 15.5 wt %, increasing the PMMA layer thickness from 1 to 3 μm led to an initial increase in flexural strength from 101 to 124 MPa, followed by a reduction to 118 MPa. The ultimate strain increased from 13.0% to 14.9% and then decreased to 13.9%. Toughness increased from 3384.5 kJ/m^3 to 5172.5 kJ/m^3, and then decreased to 4216.6 kJ/m^3. The highest mechanical performance was achieved when the PMMA layer thickness was 2 μm. The high plasticity of the PMMA "mortar" layer functions as a weak interface to arrest bridge cracks, significantly enhancing the mechanical properties. The presence of bridges connecting adjacent "brick" layers (Figure 6) facilitates stress transfer, and breakage of the bridges dissipates energy. Compared with C−S−H nacre IPH-36-15.5-3, C−S−H nacre IPH-36-15.5-2 had a thinner "mortar" layer and exhibited a higher mechanical performance. This enhancement could be attributed to the increased interface area between the PMMA "mortar" and C−S−H "brick", promoting interfacial delamination, crack deflection, and layer sliding, all of which contribute to energy dissipation. However, when the PMMA layer thickness further decreased, the flexural strength and flexural strain of C−S−H nacre IPH-36-15.5-1 decreased. The decrease could be attributed to a reduced proportion of flexible PMMA within the composite, which diminishes the stress transfer ability. The results could be utilized to design C−S−H nacres with a targeted mechanical performance.

Material Structure−Property Relationship. The fractured surfaces of cement, C−S−H-36-9.6-d, C−S−H nacre IH-36-9.6, and C−S−H nacre IPH-36-15.5-2 are shown in Figure 7. Cement showed a random microstructure with pores (Figure 7a), consistent with previous research.[70] Once a crack

https://doi.org/10.1021/acsnano.4c08200
ACS Nano 2024, 18, 23655−23671

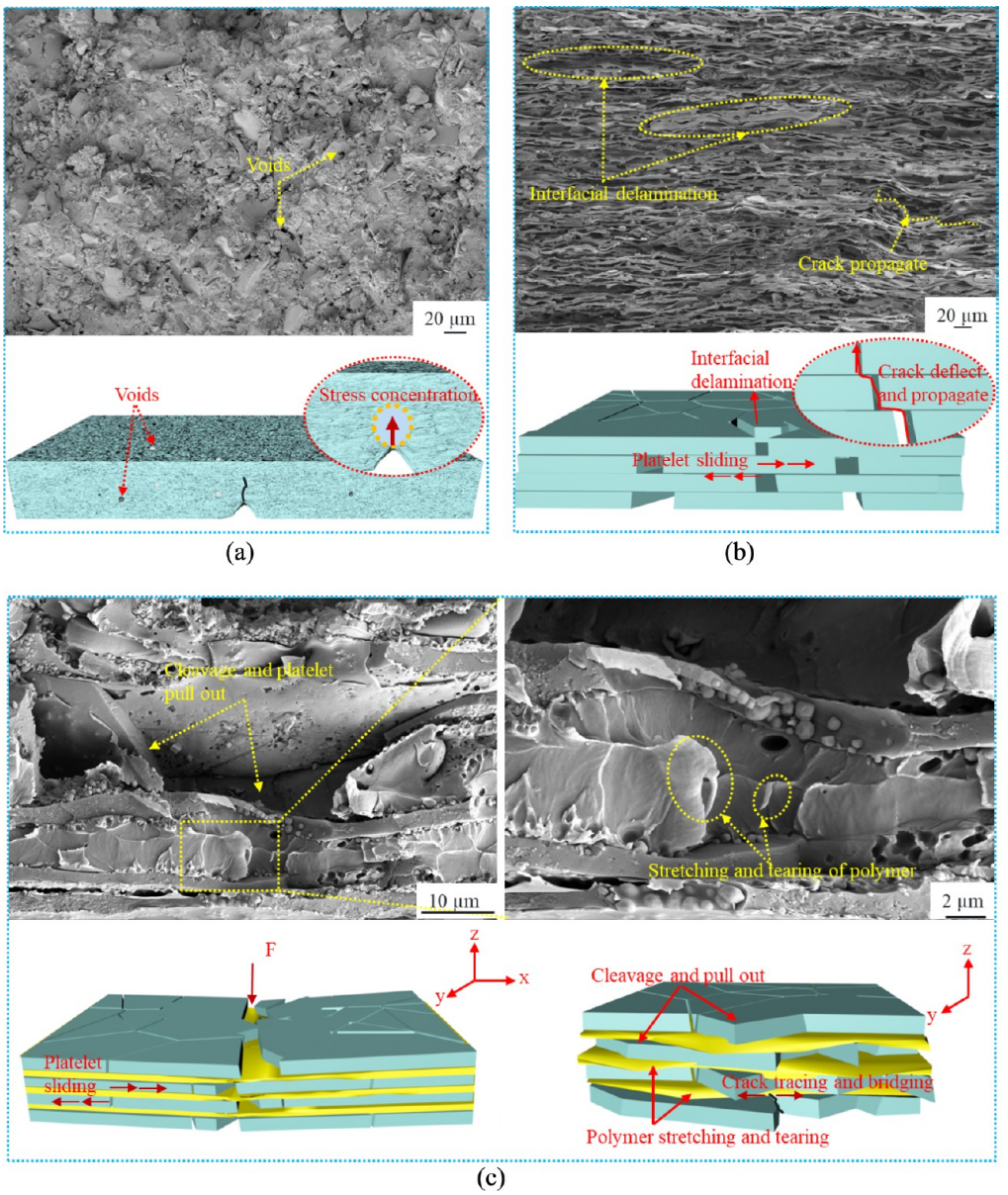

Figure 7. Fracture features and cracking behaviors: (a) cement, (b) C−S−H nacre IH-36-9.6, and (c) C−S−H nacre IPH-36-15.5-2.

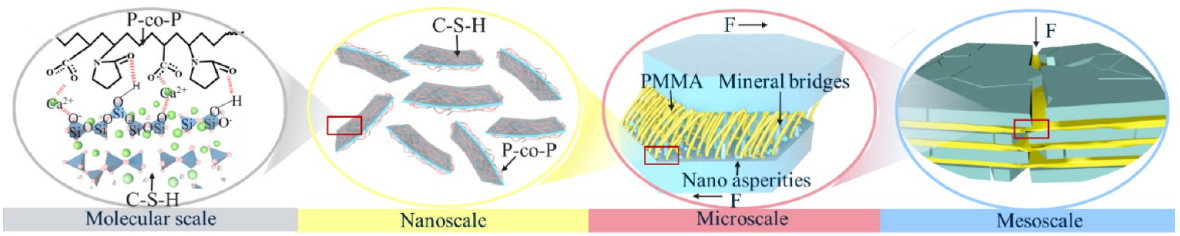

Figure 8. Underlying the toughening mechanisms of C−S−H nacre IPH at four different length scales.

is initiated at a weak spot, the crack can propagate rapidly due to the stress concentration at the crack tip. This is why cement exhibited a brittle behavior with low flexural strength and ultimate strain. C−S−H-36-9.6-d exhibited a similar fractured surface, as shown in Figure S10, which was not duplicated here.

Unlike cement and C−S−H-36-9.6-d, C−S−H nacre IH with dense hierarchical microstructures showed interfacial delamination and zigzag crack propagation, as shown in Figure 7b. The combination of delamination and crack propagation enhanced the deformability and energy dissipation capability of C−S−H nacre IH, therefore achieving higher ultimate strain and toughness than cement and C−S−H-36-9.6-d. The incorporation of P-*co*-P toughened C−S−H by hindering rapid aggregation (Figure 2), thus enhancing the crack

https://doi.org/10.1021/acsnano.4c08200
ACS Nano 2024, 18, 23655−23671

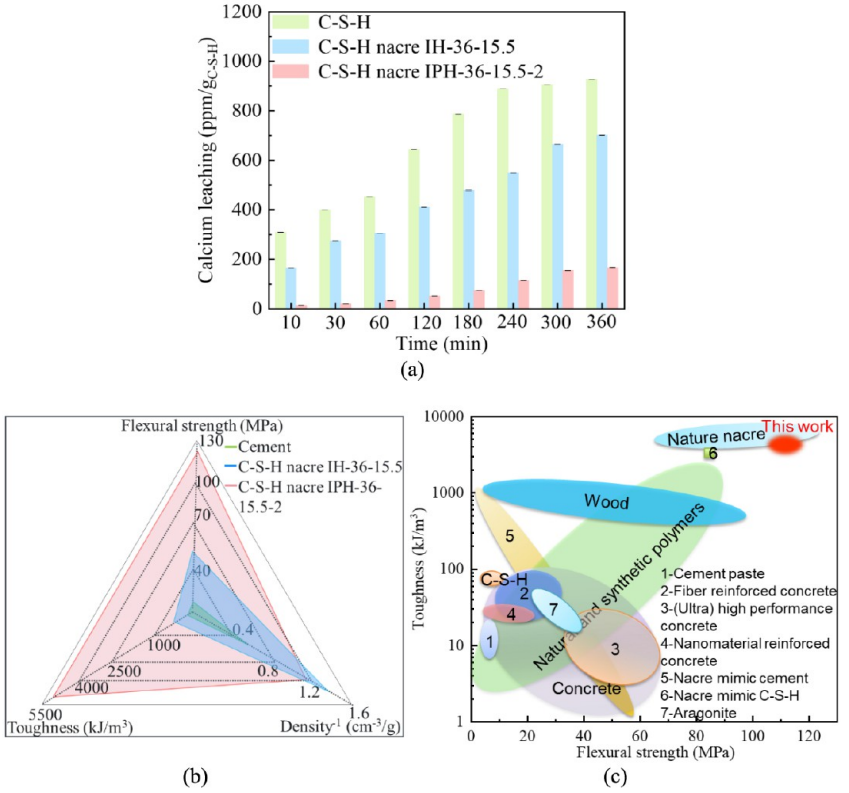

Figure 9. Durability and characteristics of C−S−H nacre: (a) calcium leaching of pure C−S−H, C−S−H nacre IH-36-15.5, and C−S−H nacre IPH-36-15.5-2; (b) density, flexural strength, and toughness comparison of C−S−H nacre IH-36-15.5, C−S−H nacre IPH-36-15.5-2, and cement paste; and (c) mechanical comparison of C−S−H nacre IPH-36-15.5-2 with common materials, including nacre, wood, polymers, C−S−H, aragonite, concrete (e.g., fiber-reinforced concrete, UHPC, and nanomaterial reinforced concrete), nacre-mimic cement-based composites, and nacre mimic C−S−H-based composites (the exact flexural strength and toughness are summarized in Table S2).

resistance of C−S−H. Excessive P-*co*-P may hinder the force transfer between C−S−H layers and reduce the strength.

As shown in Figure 7c, the fractured surface of C−S−H nacre IPH showed cleavage, indicating that a crack proceeded in the direction of the C−S−H nanoplatelets. The cracks in C−S−H nacre IPH were subsequently arrested and bridged by neighboring PMMA "mortar" layers, which effectively hindered crack propagation.[71] The stretching and tearing of PMMA, which served as a ligament bridge to span cracks and carry loads, were observed. Furthermore, the sliding of C−S−H "bricks" was observed, which could exhaust energy to increase ultimate strain and toughness. Platelet cleavage, pull out, sliding, polymer tearing, and polymer stretching collectively contributed to the high toughness observed in C−S−H nacre IPH. C−S−H nacre IPH exhibited high toughness due to the combination of C−S−H pull out and cleavage, PMMA stretching and tearing, and platelet sliding.

The investigations described above indicate that the dense "brick-and-mortar" microstructure of C−S−H nacre IPH plays important roles in enhancing the mechanical performance. The mechanisms are summarized in Figure 8, where the P-*co*-P exhibits strong interfacial interactions with C−S−H through calcium ion coordination bonds and hydrogen bonds at the molecular scale. Besides, the P-*co*-P provides intrinsic effects via toughening the C−S−H "brick" layers, thus inhibiting crack initiation and propagation at nano- to microscales. Meanwhile, the breaking of mineral bridges, inelastic shearing resisted by asperities, and stable interlocking provided by waviness during sliding contribute significantly to enhancement of the overall mechanical performance. Furthermore, the PMMA "mortar" layers offer extrinsic effects via toughening the matrix at micro- to mesoscales to impede crack propagation.[43]

Durability and Mechanical Comparison with Other Materials. The calcium leaching of C−S−H nacres was investigated because it plays a significant role in the durability of cementitious materials in harsh environments involving seawater attack, acid attack, or sulfate acid.[72,73] Different C−S−H-based materials were added to water, and the calcium leaching test results are shown in Figure 9a. When pure C−S−H was added, the calcium ion concentration rapidly increased, with values reaching as high as 300 ppm within 10 min. In contrast, when C−S−H nacre IH and C−S−H nacre IPH were added, the increase in calcium ion concentration was slow. After 360 min, the calcium ion leaching concentration of C−S−H nacre IPH was 5.5 times lower than that of pure C−S−H, indicating that C−S−H nacre had high resistance to decalcification. The calcium leaching results imply the enhanced durability of C−S−H nacre. The durability can be attributed to the highly ordered, dense "brick-and-mortar" microstructure.

The mechanical properties and densities of C−S−H nacre are shown in Figures 9b and S11. Compare the mechanical performance of C−S−H nacre with that of other materials, as shown in Figure 9c. C−S−H nacre IPH showed flexural performance: flexural strength = 124 MPa, toughness = 5173 kJ/m^3, and density = 0.98 g/cm^3, comparable to that of natural nacre. The flexural strength and toughness of C−S−H nacre IPH were 18 and 1230 times, respectively, higher than those of

https://doi.org/10.1021/acsnano.4c08200
ACS Nano 2024, 18, 23655−23671

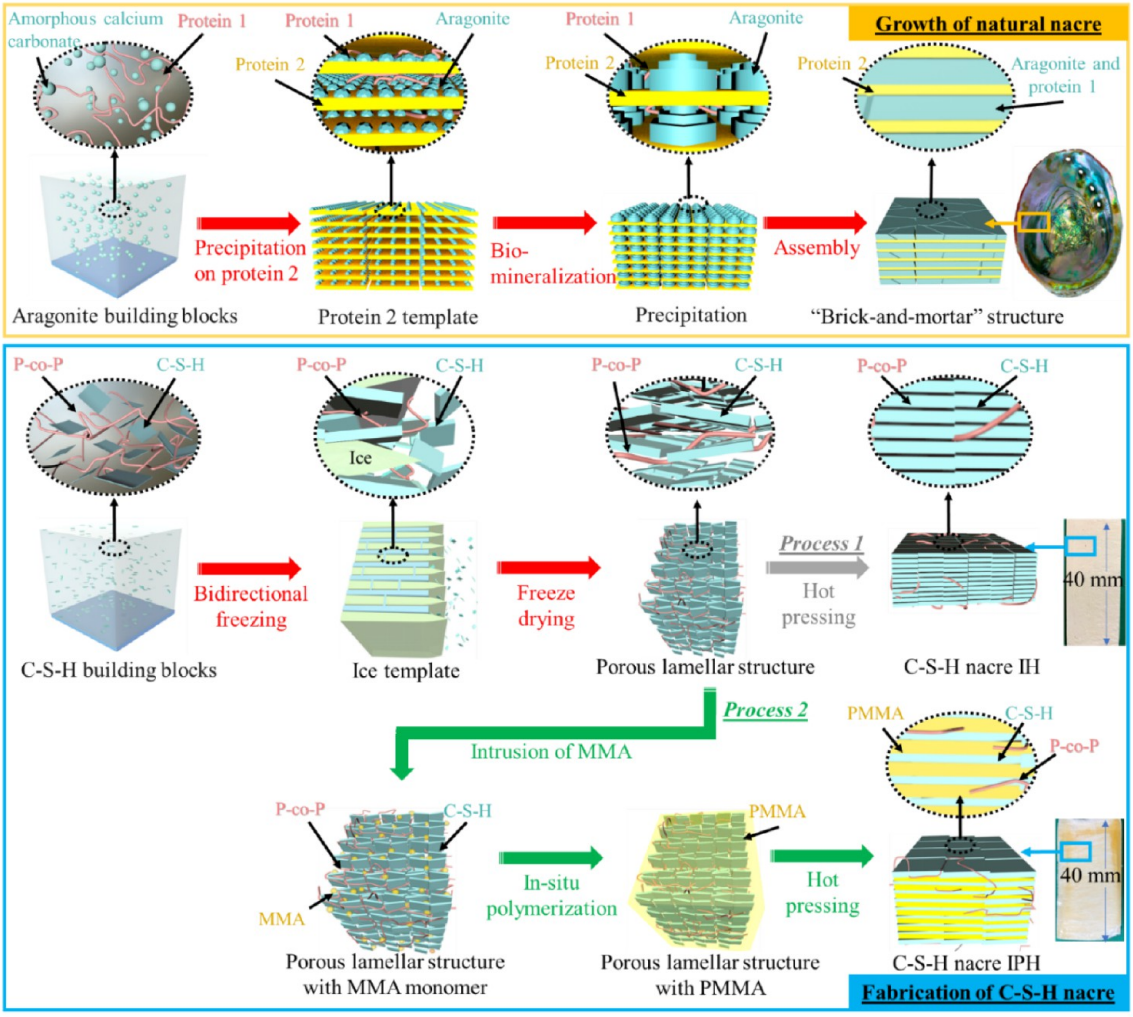

Figure 10. Growth process of natural nacre and nacre-inspired processes for fabricating C−S−H nacre.

cement paste (7 MPa and 4.2 kJ/m^3), while the density was reduced by 60%. The flexural strength and toughness of C−S−H nacre IPH are higher than those of other nacre-mimicking cementitious materials, which typically have flexural strengths ranging from 3 to 58 MPa and toughness ranging from 0.23 to 1470 kJ/m^3. C−S−H nacre IPH outperformed polymer/nanoparticle/fiber-reinforced concrete with flexural strengths ranging from 6 to 41 MPa and toughness ranging from 1 to 1200 kJ/m^3. The exceptional mechanical properties offer possibilities for using C−S−H nacre as an ultrahigh-performance material to revolutionize the construction industry.

CONCLUSIONS

This paper presents innovative methods for fabricating C−S−H nacre with a dense "brick-and-mortar" microstructure and high mechanical properties. The effects of material constitution, fabrication process, and microstructures on the flexural properties and durability of C−S−H nacre have been evaluated. The test data have been utilized to establish a material process−structure−property relationship for C−S−H nacre, facilitating the design of ultrahigh-performance C−S−H-based and cement-based composites for engineering applications. Based on the above investigation, the following conclusions are drawn:

- The proposed method (freeze casting, freeze-drying, in situ polymerization, and hot pressing) is effective in fabricating C−S−H nacre with dense "brick-and-mortar" hierarchical microstructures. C−S−H building blocks with porous hierarchical microstructures have been fabricated via freeze casting and freeze-drying. C−S−H nacre IH samples with dense hierarchical microstructures have been fabricated through hot pressing porous C−S−H building blocks. C−S−H nacre IPH samples with dense "brick-and-mortar" hierarchical microstructures have been fabricated via intruding MMA into porous C−S−H building blocks, followed by in situ polymerization and hot pressing. The thickness of "brick" and "mortar" layers, along with the presence of mineral bridges, waviness, and asperities, could be modified by adjusting fabrication process parameters such as P-*co*-P, C−S−H, and PMMA.
- The fabricated C−S−H nacre achieved high flexural strength, high toughness, and lightweight simultaneously. The C−S−H nacre IH achieved higher flexural strength (53 MPa) and toughness (515.5 kJ/m^3) compared with cement paste and disordered C−S−H. The C−S−H nacre IPH achieved outstanding flexural strength (124 MPa), high toughness (5173 kJ/m^3), and low density (0.98 g/cm^3). The flexural strength and

https://doi.org/10.1021/acsnano.4c08200
ACS Nano 2024, 18, 23655−23671

Table 1. Parameters for Synthesizing C−S−H Building Blocks

designation	$CaCl_2$ concentration (mmol/L)	Na_2SiO_3 concentration (mmol/L)	P-*co*-P content (wt %)	C−S−H content (wt %)
C−S−H	60	60	0	9.6
C−S−H-36-9.6-d	60	60	36	9.6
C−S−H nacre IH-17-9.6	60	60	17	9.6
C−S−H nacre IH-23-9.6	60	60	23	9.6
C−S−H nacre IH-30-9.6	60	60	30	9.6
C−S−H nacre IH-36-9.6	60	60	36	9.6
C−S−H nacre IH-40-9.6	60	60	40	9.6
C−S−H nacre IH-36-3.2	30	30	36	3.2
C−S−H nacre IH-36-15.5	90	90	36	15.5
C−S−H nacre IH-36-20.2	120	120	36	20.2

toughness of C−S−H nacre IPH surpass cement paste by 18 and 1230 times, respectively, while achieving a 60% reduction in density. These mechanical properties outstrip existing cementitious materials and natural nacre. The flexural properties of C−S−H nacre are closely related to the polymer content, C−S−H content, and hierarchical microstructure. Optimizing these parameters improves mechanical properties, thereby enhancing the suitability of the proposed material for various engineering applications. Moreover, calcium leaching tests validated the enhanced durability of C−S−H nacre.

- The enhancement in mechanical performance and durability is attributed to the dense "brick-and-mortar" microstructure of C−S−H nacre. P-*co*-P has been used to toughen C−S−H building blocks functioning as "brick" to provide mechanical strength. PMMA functions as "mortar" to arrest and deflect cracks, enhancing toughness. In addition, the presence of mineral bridges, asperities, and waviness further enhances mechanical performance by arresting and deflecting cracks. The other toughening mechanisms, including platelet pull out, interlayer sliding, polymer stretching, and polymer tearing, can further improve the mechanical performance of C−S−H nacre.

METHODS AND EXPERIMENTAL

Fabrication of C−S−H Nacre. Inspired by the "brick-and-mortar" microstructure of natural nacre, we have proposed methods for fabricating C−S−H nacre in Figure 10. The growth of natural nacre involves the creation of aragonite building blocks, which include amorphous calcium carbonate and protein 1. These blocks evolve through a continuous nucleation process, with the amorphous calcium carbonate precursor being regulated by protein 1. Subsequently, within the scaffold provided by protein 2, the aragonite blocks orderly form and expand until the space of the scaffold is fully occupied.[67]

This research investigated two nacre-inspired processes that produce different C−S−H nacres. Both processes share the initial steps of C−S−H building block creation, ice template preparation, and porous lamellar structure assembly. Once the porous lamellar structure is fabricated, the first process concludes with a hot pressing technique. In contrast, the second process intrudes poly(methyl methacrylate) (PMMA) before executing the hot pressing. The incorporation of PMMA ensures that the produced C−S−H nacre embodies an interlayer of PMMA between the C−S−H layers, mimicking the "brick-and-mortar" structure of natural nacre. The two C−S−H nacres fabricated via the two processes are designated as C−S−H nacre IH (ice-templating and hot-pressing) and C−S−H nacre IPH (ice-templating, polymerization, and hot-pressing), respectively.

Generation of C−S−H Building Blocks. C−S−H building blocks were produced via coprecipitation with $CaCl_2$ and Na_2SiO_3.[74,75] The challenge of producing C−S−H building blocks is that C−S−H rapidly precipitates as gels with random microstructures due to internal electrostatic repulsion.[76] To tackle this challenge, poly(acrylamide-*co*-acrylic acid) (or P-*co*-P in short) with an M_w of 520 000 was utilized to stabilize C−S−H and mitigate the random precipitation of C−S−H. The use of P-*co*-P mimics the generation of aragonite building blocks, combining aragonite and protein 1 found in natural nacre (as depicted in Figure 10). The minimum P-*co*-P content required to stabilize C−S−H was determined as 17 wt % through iterative TGA tests. This crucial threshold establishes the baseline for the P-*co*-P content in subsequent experiments. The coprecipitation process includes three main steps:

(1) Add P-*co*-P solution (10 mg/mL) into Na_2SiO_3 solution (60 mmol/L) dropwise. Magnetic stirring was performed throughout this step.
(2) Add $CaCl_2$ solution (60 mmol/L) into the mixture dropwise under magnetic stirring. The $CaCl_2$ and Na_2SiO_3 contents were adjusted to maintain a calcium to silicate ratio of 1.1 for the production of C−S−H building blocks, consistent with references[25] and[77].
(3) Stir the mixture for 12 h to ensure full precipitation of C−S−H building blocks.

With the above method, C−S−H building block suspensions with different P-*co*-P contents (17, 23, 30, 36, and 40 wt %) and C−S−H contents (3.2 wt %, 9.6 wt %, 15.5%, and 20.2 wt %) were prepared and used to evaluate the effects of C−S−H and P-*co*-P contents on the microstructures and mechanical properties of C−S−H nacre. The C−S−H content was adjusted via changing the concentrations of Na_2SiO_3 and $CaCl_2$ solutions. The C−S−H content was quantified by measuring the masses of samples after freeze-drying. The parameters of different suspensions and their designations are listed in Table 1.

C−S−H nacre IH-0-9.6, C−S−H nacre IH-17-9.6, C−S−H nacre IH-23-9.6, C−S−H nacre IH-30-9.6, C−S−H nacre IH-36-9.6, and C−S−H nacre IH-40-9.6 with the same C−S−H content (9.6 wt %) and different P-*co*-P contents (0, 17, 23, 30, 36, and 40 wt %) were designed to evaluate the effect of P-*co*-P content. C−S−H nacre IH-36-3.2, C−S−H nacre IH-36-9.6, C−S−H nacre IH-36-15.5, and C−S−H/P-c-P-36-20.2 with the same P-*co*-P content (36 wt %) and different C−S−H

https://doi.org/10.1021/acsnano.4c08200
ACS Nano 2024, 18, 23655−23671

contents (3.2, 9.6, 15.5, and 20.2 wt %) were designed to evaluate the effect of C−S−H content. The suspensions were stored in a glovebox filled with nitrogen. The temperature was kept at 25 ± 1 °C. Deionized water was boiled before the synthesis. The pH of all suspensions was adjusted to 11.2 ± 0.1 using NaOH (1 mol/L), consistent with the reference[55].

Preparation of the Lamellar Structure. The produced C−S−H building block suspensions were utilized to prepare laminated structures via bidirectional freeze casting. First, the suspensions were cooled to 4 °C, sonicated to remove air bubbles, and then poured into a polydimethylsiloxane (PDMS, Dow Corning Sylgard 184) mold, which was attached to a copper plate. The internal dimensions of the PDMS mold were 40 × 40 × 40 mm^3. One side of the copper plate was immersed in liquid nitrogen, and the other side of the copper plate was exposed to the ambient environment, creating temperature gradients along the horizontal (ΔT_H) and vertical (ΔT_V) directions of the PDMS mold, which has low thermal conductivity. Since ice crystal preferentially grows along temperature gradients, C−S−H building blocks were expelled from the freezing suspension and replicated a lamellar ice pattern (Figure 10).

After the C−S−H building block suspension was frozen, the solid cube was moved out of the PDMS molds and then dried using a freeze-dryer (Labconco, FreeZone 6L −50 °C Complete Freeze-Dryer System) for the removal of ice. The samples were dried by using a freeze-dryer to minimize the impact on the microstructures.

For comparison, samples with disordered C−S−H scaffold (designated as C−S−H-36-9.6-d) were fabricated via freezing C−S−H suspension with 36 wt % P-*co*-P and 9.6 wt % of C−S−H in a PDMS mold subjected to liquid nitrogen, followed by freeze-drying and hot pressing. Cement paste was prepared via mixing Type I Portland cement with tap water at a water-to-cement ratio of 0.5. The cement paste was used to cast cube samples, and the samples were cured at room temperature (25 °C) in lime-saturated water for 28 days prior to mechanical testing.

Introduction of PMMA. In the second fabrication process proposed in this research, PMMA was utilized to generate "mortar" layers, which mimic the "brick-and-mortar" architecture of natural nacre. The introduction of PMMA involved three main steps:

(1) Initial polymerization: Methyl methacrylate (MMA) monomer (Thermal Scientific, CAS: 80-62-6) was initiated by 1 wt % of 2,2-azobis(isobutyronitrile) (AIBN) (Sigma Aldrich, CAS 78-67-1) in a water bath with magnetic stirring. The temperature of the water bath was maintained at 80 °C.

(2) Polymerization propagation: PMMA is produced via in situ polymerization of the MMA monomer, accompanied by the increase of the viscosity of the solution. After the viscosity increased to a critical level that corresponds to a prepolymerization of the monomer,[78] the solution was poured into a cubic mold with a C−S−H nacre IH-36-15.5 porous lamellar structure samples inside. The mold was then placed in a vacuum oven, and the temperature of the vacuum oven was kept at 40 °C for 24 h.

(3) Polymerization termination: The temperature of the vacuum oven for polymerization was increased from 40 to 80 °C, and the high temperature was kept for 2 h.

This research investigated C−S−H nacre IPH with different thicknesses (1, 3, and 5 μm) of PMMA, designated as C−S−H nacre IPH-36-15.5-1, C−S−H nacre IPH-36-15.5-2, and C−S−H nacre IPH-36-15.5-3, aiming to evaluate the effect of PMMA thickness on the mechanical properties. The thickness of PMMA was regulated by adjusting the gaps between adjacent layers in the C−S−H porous lamellar structure with 36 wt % P-*co*-P and 15.5 wt % C−S−H. The interlayer gaps were adjusted using steel plates with different thicknesses in the hot pressing process, as illustrated in Figure S1. Details about the P-*co*-P content, C−S−H content, and PMMA thickness of the C−S−H nacre IPH are shown in Table 2.

Table 2. Parameters for Synthesizing C−S−H Nacre IPH

designation	P-*co*-P content (wt %)	C−S−H content (wt %)	PMMA thickness (μm)
C−S−H nacre IPH-36-15.5-1	36	15.5	1
C−S−H nacre IPH-36-15.5-2	36	15.5	3
C−S−H nacre IPH-36-15.5-3	36	15.5	5

Hot Pressing. The C−S−H nacre samples in the two fabrication processes were densified via hot pressing. The pressure for both C−S−H nacre IH and C−S−H nacre IPH was set to 10 MPa. The temperature was kept at 100 °C for C−S−H nacre IH and at 130 °C for C−S−H nacre IPH. The temperature values (100 and 130 °C) were determined by the softening points of P-*co*-P and PMMA.[79,80] The temperature and pressure were maintained for 30 min.

Characterization. The cross sections and fracture surfaces of porous lamellar structures and C−S−H nacres were inspected using a scanning electron microscope (SEM, Zeiss Auriga FIB/SEM) at a 5 kV voltage. To inspect the cross section, the porous lamellar structure was cut and C−S−H nacre samples were fractured in liquid nitrogen. To inspect the fracture surface after loading, C−S−H nacres were taken from the specimens fractured in three-point bending tests. All samples were sputtered with Au for 90 s to achieve an appropriate conductivity. The wall density and wall thickness were evaluated with SEM images, and five duplicates were conducted for each sample.

Three-point bending tests were conducted to evaluate the flexural properties of C−S−H nacres using a universal testing machine (Instron load frame 5581, USA). The samples were 40 mm in length, 5 mm in width, and 2 mm in thickness. The load cell had a capacity of 500 N, and the loading rate was set at 0.1 mm/min. The surfaces of the test samples were polished by using silicon carbide (SIC) papers. Each test was replicated five times. According to ASTM D790-03,[81] the flexural stress (σ) and flexural strain (ε) were calculated using eq 1:

$$\sigma = \frac{3FL}{2bd^2} \tag{1a}$$

$$\varepsilon = \frac{6Dd}{L^2} \tag{1b}$$

where F is the applied force (unit: N); L is the span length (L = 20 mm); b is the width of samples (b = 5 mm); d is the thickness of samples (d = 2 mm); and D is the midspan deflection (unit: mm). Flexural strength is defined as the peak flexural stress. Ultimate strain is defined as the flexural strain

https://doi.org/10.1021/acsnano.4c08200
ACS Nano 2024, 18, 23655−23671

when the sample fails. Toughness is the area of the flexural stress versus flexural strain curve normalized by the area of the fracture surface.

Fourier transform infrared spectroscopy (FTIR, model: Bruker Optics Tensor 27 Fourier Transform Infrared Spectrometer) was applied to evaluate the chemical structures and interactions of C−S−H, P-*co*-P, and C−S−H nacre IH. All samples were subjected to vacuum drying for 24 h before testing, followed by thorough mixing with KBr powder, and subsequently compressed into pellets. The spectra wavenumbers start from 400 to 4000 cm^{-1}.

The morphology of C−S−H was visually inspected by using a transmission electron microscope (TEM, JEOL 2100 Plus 200 keV). Different C−S−H samples were prepared with or without the presence of P-*co*-P. To prepare the samples, C−S−H suspensions were dispersed on a carbon-coated copper grid (etching for 30 s prior to use). Prior to dispersion, all suspensions were sonicated for 10 min. Subsequently, all of the samples were dried in air for 15 min before testing.

Thermogravimetric analysis (TGA) was conducted using a thermal analyzer (TA 187 TG55) to assess the polymer content and thermal properties of C−S−H, PMMA, and C−S−H nacres. To prepare the test samples, the specimens fractured in the bending tests were cut into small pieces and then milled into a fine powder. The powder samples were vacuum-dried for 24 h before testing. The TGA test involved heating the samples at a constant rate of 20 °C/min, ranging from 30 to 1000 °C, in a flow of nitrogen at 50 mL/min.

Dynamic light scattering (DLS) tests were carried out to assess the stability of C−S−H, P-*co*-P, and C−S−H building blocks using a DLS analyzer (model: Zetasizer Nano ZS90, Malvern Instruments Ltd., UK) based on the zeta potential. Each measurement involved three readings at 25 °C, and the average value was calculated. Prior to the test, all suspensions, prepared at a concentration of 0.1 g/L, were homogenized via bath sonication for 15 min.

The density (ρ) of each sample was evaluated by eq 2:

$$\rho = \frac{m}{V} \tag{2}$$

where m is the mass (unit: g) and V is the volume (unit: cm^3).

The calcium leaching experiment was carried out using an Inductively Coupled Plasma-Optical Emission Spectrometer (ICP-OES, Agilent 5100). For the sample preparation, 0.1 g each of C−S−H, C−S−H IH-15.5-36, and C−S−H IH-15.5-36-2 were added into 100 mL of deionized (DI) water, followed by thorough stirring. At specific time intervals, 5 mL of the solution was collected via vacuum filtration and then acidified with nitric acid. Calibration of the equipment was performed by preparing calcium standards with concentrations of 0, 1, 5, 10, 50, 80, and 100 ppm through dilution of a 1000 ppm calcium standard for ICP.

The XRD test was carried out using a Cu K radiation source (model: Rigaku Ultima IV X-ray diffractometer, 40 kV, 40 mA) to evaluate the crystalline structures of the C−S−H and C−S−H nacre composite. The C−S−H and C−S−H nacre IH-17-9.6 samples were milled into a powder. During the XRD tests, each powder sample was scanned on a rotating stage between 2° and 60° (2θ). The step size of scanning was 0.02°, and the time per step was 30 s.

Micro-CT analysis was performed to investigate the microstructure of C−S−H nacre IPH using a SKYSCAN 1272 instrument (Bruker). C−S−H nacre IPH-36-15.5-3 samples for micro-CT were prepared by polishing the sample surface using sandpaper. The samples were installed on a holder to maintain stability during the scan. Prior to scanning, the micro-CT scanner settings were adjusted, including a resolution of 1024 × 1024 and a full rotation step of 360°, ensuring optimal X-ray penetration through the sample. Adjustments to the X-ray voltage and current were facilitated by modifying the filter settings. The data reconstruction process utilized NRecon and CTAn software to transform the 2D images into a 3D model.

ASSOCIATED CONTENT

Supporting Information

The Supporting Information is available free of charge at https://pubs.acs.org/doi/10.1021/acsnano.4c08200.

Flexural properties (Table S1), illustration of hot pressing process (Figure S1); SEM image of C-S-H-36-9.6-d (Figure S2); photo of different sizes of C−S−H samples (Figure S3); TGA curves of C−S−H nacre IH samples with different P-*co*-P contents (Figure S4); TGA curves of C−S−H nacre IPH under different PMMA thicknesses (Figure S5); SEM image of the top surface and cross section of the C−S−H nacre IPH-36-15.5-2 (Figure S6); EDS maps of C−S−H nacre IPH-36-15.5-2 (Figure S7); lower magnification SEM image of IPH-36-15.5-2 (Figure S8); micro-CT images of C−S−H nacre IPH (Figure S9); SEM image of the fracture surface of C−S−H-36-9.6-d (Figure S10); C−S−H nacre IPH standing on the leaf (Figure S11); flexural and toughness of polymers, wood, concrete, and aragonite(Table S2) (PDF)

AUTHOR INFORMATION

Corresponding Author

Weina Meng − *Department of Civil, Environmental and Ocean Engineering, Stevens Institute of Technology, Hoboken, New Jersey 07030, United States*; Email: wmeng3@stevens.edu

Authors

Yuhuan Wang − *Department of Civil, Environmental and Ocean Engineering, Stevens Institute of Technology, Hoboken, New Jersey 07030, United States*; orcid.org/0000-0001-6375-2670

Yi Bao − *Department of Civil, Environmental and Ocean Engineering, Stevens Institute of Technology, Hoboken, New Jersey 07030, United States*

Complete contact information is available at: https://pubs.acs.org/10.1021/acsnano.4c08200

Notes

The authors declare no competing financial interest.

ACKNOWLEDGMENTS

This research was funded by the National Science Foundation [award no. CMMI 2046407]. The authors thank Dr Tsengming Chou for helping with the SEM, TEM, and micro-CT tests. The authors thank the Laboratory for Multiscale Imaging for generously providing liquid nitrogen.

REFERENCES

(1) Oorkalan, A.; Chithra, S.; Balaji, R.; Kumar, S. G.; Kumar, J. K.; Kumar, T. K. Experimental Study on High Volume Fly Ash Concrete Made with Coir Pith and Quarry Dust. *Mater. Today: proc.* **2020**, *21*, 833−836.

(2) Brara, A.; Klepaczko, J. Experimental Characterization of Concrete in Dynamic Tension. *Mech. Mater.* **2006**, *38* (3), 253−267.

(3) Li, V. C.; Maalej, M. Toughening in Cement Based Composites. Part I: Cement, Mortar, and Concrete. *J. Cem. Concr. Compos.* **1996**, *18* (4), 223−237.

(4) Hoseini, M.; Bindiganavile, V.; Banthia, N. The Effect of Mechanical Stress on Permeability of Concrete: A Review. *J. Cem. Concr. Compos.* **2009**, *31* (4), 213−220.

(5) Grassl, P. A Lattice Approach to Model Flow in Cracked Concrete. *J. Cem. Concr. Compos.* **2009**, *31* (7), 454−460.

(6) Maruyama, I.; Lura, P. Properties of Early-Age Concrete Relevant to Cracking in Massive Concrete. *Cem. Concr. Res.* **2019**, *123*, 105770.

(7) Ye, H.; Tian, Y.; Jin, N.; Jin, X.; Fu, C. Influence of Cracking on Chloride Diffusivity and Moisture Influential Depth in Concrete Subjected to Simulated Environmental Conditions. *Constr. Build. Mater.* **2013**, *47*, 66−79.

(8) Banthia, N.; Gupta, R. Influence of Polypropylene Fiber Geometry on Plastic Shrinkage Cracking in Concrete. *Cem. Concr. Res.* **2006**, *36* (7), 1263−1267.

(9) Shen, D.; Liu, C.; Luo, Y.; Shao, H.; Zhou, X.; Bai, S. Early-Age Autogenous Shrinkage, Tensile Creep, and Restrained Cracking Behavior of Ultra-High-Performance Concrete Incorporating Polypropylene Fibers. *J. Cem. Concr. Compos.* **2023**, *138*, 104948.

(10) Bui, H. T.; Maekawa, K.; Tan, K. H. Microcell and Macrocell Corrosion of Steel Bars in Reinforced Concrete Slabs Under Different Corrosive Environments and Cathode/Anode Configurations. *J. Cem. Concr. Compos.* **2023**, *138*, 104989.

(11) Berrocal, C. G.; Lundgren, K.; Löfgren, I. Corrosion of Steel Bars Embedded in Fibre Reinforced Concrete Under Chloride Attack: State of the Art. *Cem. Concr. Res.* **2016**, *80*, 69−85.

(12) Lee, J.-H.; Cho, B.; Choi, E. Flexural Capacity of Fiber Reinforced Concrete with A Consideration of Concrete Strength and Fiber Content. *Constr. Build. Mater.* **2017**, *138*, 222−231.

(13) Ding, Y.; Wang, Q.; Pacheco-Torgal, F.; Zhang, Y. Hybrid Effect of Basalt Fiber Textile and Macro Polypropylene Fiber on Flexural Load-Bearing Capacity and Toughness of Two-Way Concrete Slabs. *Constr. Build. Mater.* **2020**, *261*, 119881.

(14) Teng, L.; Khayat, K. H. Effect of Overlay Thickness, Fiber Volume, and Shrinkage Mitigation on Flexural Behavior of Thin Bonded Ultra-High-Performance Concrete Overlay Slab. *J. Cem. Concr. Compos.* **2022**, *134*, 104752.

(15) Khayat, K. H.; Meng, W. Nanotechnology for Civil Infrastructure: Innovation and Eco-Efficiency of Nanostructured Cement-Based MaterialsElsevier2023.

(16) Meng, W.; Khayat, K. H. Design, Mechanism, and Performance of Cement-Based Materials with 1D Nanomaterials. *Nanotechnol. Civil Infrast.* **2023**, 93−126.

(17) Cho, B. H.; Nam, B. H.; Khawaji, M. Flexural Fatigue Behaviors and Damage Evolution Analysis of Edge-Oxidized Graphene Oxide (EOGO) Reinforced Concrete Composites. *J. Cem. Concr. Compos.* **2021**, *122*, 104082.

(18) Douba, A.; Hou, P.; Kawashima, S. Hydration and Mechanical Properties of High Content Nano-Coated Cements with Nano-Silica, Clay and Calcium Carbonate. *Cem. Concr. Res.* **2023**, *168*, 107132.

(19) Meng, W.; Khayat, K. H. Mechanical Properties of Ultra-High-Performance Concrete Enhanced with Graphite Nanoplatelets and Carbon Nanofibers. *Compos., Part B* **2016**, *107*, 113−122.

(20) Lu, D.; Ma, L.-P.; Zhong, J.; Tong, J.; Liu, Z.; Ren, W.; Cheng, H.-M. Growing Nanocrystalline Graphene on Aggregates for Conductive and Strong Smart Cement Composites. *ACS Nano* **2023**, *17* (4), 3587−3597.

(21) Wang, R.; Wang, P.-M.; Li, X.-G. Physical and Mechanical Properties of Styrene−Butadiene Rubber Emulsion Modified Cement Mortars. *Cem. Concr. Res.* **2005**, *35* (5), 900−906.

(22) Liang, R.; Liu, Q.; Hou, D.; Li, Z.; Sun, G. Flexural Strength Enhancement of Cement Paste through Monomer Incorporation and *In Situ* Bond Formation. *Cem. Concr. Res.* **2022**, *152*, 106675.

(23) Richardson, I. G. The Calcium Silicate Hydrates. *Cem. Concr. Res.* **2008**, *38* (2), 137−158.

(24) Allen, A. J.; Thomas, J. J.; Jennings, H. M. Composition and Density of Nanoscale Calcium−Silicate−Hydrate in Cement. *Nat. Mater.* **2007**, *6* (4), 311−316.

(25) Picker, A.; Nicoleau, L.; Burghard, Z.; Bill, J.; Zlotnikov, I.; Labbez, C.; Nonat, A.; Cölfen, H. Mesocrystalline Calcium Silicate Hydrate: A Bioinspired Route Toward Elastic Concrete Materials. *Sci. Adv.* **2017**, *3* (11), No. e1701216.

(26) Li, Y.; Li, H.; Jin, C.; Wang, Z.; Hao, J.; Li, Y.; Liu, J. Multi-Scale Investigation and Mechanism Analysis on Young's Modulus of CSH Modified by Multi-Walled Carbon Nanotubes. *Constr. Build. Mater.* **2021**, *308*, 125079.

(27) de Souza, F. B.; Shamsaei, E.; Chen, S.; Sagoe-Crentsil, K.; Duan, W. Controlled Growth and Ordering of Poorly-Crystalline Calcium-Silicate-Hydrate Nanosheets. *Commun. Mater.* **2021**, *2* (1), 84.

(28) Mansur, A. A.; Mansur, H. S. Preparation, Characterization and Cytocompatibility of Bioactive Coatings on Porous Calcium-Silicate-Hydrate Scaffolds. *Mater. Sci. Eng.* **2010**, *30* (2), 288−294.

(29) Wu, J.; Zhu, Y. J.; Cao, S. W.; Chen, F. Hierachically Nanostructured Mesoporous Spheres of Calcium Silicate Hydrate: Surfactant-Free Sonochemical Synthesis and Drug-Delivery System with Ultrahigh Drug-Loading Capacity. *Adv. Mater.* **2010**, *22* (6), 749−753.

(30) Wu, J.; Zhu, Y. J.; Chen, F. Ultrathin Calcium Silicate Hydrate Nanosheets with Large Specific Surface Areas: Synthesis, Crystallization, Layered Self-Assembly and Applications as Excellent Adsorbents for Drug, Protein, and Metal Ions. *Small* **2013**, *9* (17), 2911−2925.

(31) Shao, N.; Tang, S.; Liu, Z.; Li, L.; Yan, F.; Liu, F.; Li, S.; Zhang, Z. Hierarchically Structured Calcium Silicate Hydrate-Based Nanocomposites Derived From Steel Slag for Highly Efficient Heavy metal Removal from Wastewater. *ACS Sustainable Chem. Eng.* **2018**, *6* (11), 14926−14935.

(32) Chen, H.; Yuan, X.; Xiong, T.; Jiang, L.; Wang, H.; Wu, Z. Biochar Facilitated Hydroxyapatite/Calcium Silicate Hydrate for Remediation of Heavy Metals Contaminated Soils. *Water, Air, Soil Pollut.* **2020**, *231* (2), 1−16.

(33) Li, J.; Zhang, J.; Wu, X.; Zhao, J.; Wu, M.; Huan, W. A Nanocomposite Paper Comprising Calcium Silicate Hydrate Nanosheets and Cellulose Nanofibers for High-Performance Water Purification. *RSC Adv.* **2020**, *10* (51), 30304−30313.

(34) Shamsaei, E.; Basquiroto de Souza, F.; Fouladi, A.; Sagoe-Crentsil, K.; Duan, W. Graphene Oxide-Based Mesoporous Calcium Silicate Hydrate Sandwich-Like Structure: Synthesis and Application for Thermal Energy Storage. *ACS Appl. Energy Mater.* **2022**, *5* (1), 958−969.

(35) Du, F.; Jin, Z.; Yang, R.; Hao, M.; Wang, J.; Xu, G.; Zuo, W.; Geng, Z.; Pan, H.; Li, T. Thermally Insulating and Fire-Retardant Bio-Mimic Structural Composites With a Negative Poisson's Ratio for Battery Protection. *Carbon Energy* **2023**, *5* (12), No. e353.

(36) Du, F.; Zhu, W.; Yang, R.; Zhang, Y.; Wang, J.; Li, W.; Zuo, W.; Zhang, L.; Chen, L.; She, W. Bioinspired Super Thermal Insulating, Strong and Low Carbon Cement Aerogel for Building Envelope. *Adv. Sci.* **2023**, *10* (18), 2300340.

(37) Abdolhosseini Qomi, M.; Krakowiak, K.; Bauchy, M.; Stewart, K.; Shahsavari, R.; Jagannathan, D.; Brommer, D. B.; Baronnet, A.; Buehler, M. J.; Yip, S. Combinatorial Molecular Optimization of Cement Hydrates. *Nat. Commun.* **2014**, *5* (1), 4960.

(38) Kai, M.; Zhang, L.; Liew, K. Graphene and Graphene Oxide in Calcium Silicate Hydrates: Chemical Reactions, Mechanical Behavior and Interfacial Sliding. *Carbon* **2019**, *146*, 181−193.

https://doi.org/10.1021/acsnano.4c08200
ACS Nano 2024, 18, 23655−23671

(39) Yu, Z.; Zhou, A.; Lau, D. Mesoscopic Packing of Disk-like Building Blocks in Calcium Silicate Hydrate. *Sci. Rep.* **2016**, *6* (1), 36967.
(40) Liu, K.; Cheng, X.; Ma, Y.; Gao, X.; Zhang, C.; Li, Z.; Zhuang, J. Analysis of Interfacial Nanostructure and Interaction Mechanisms Between Cellulose Fibres and Calcium Silicate Hydrates Using Experimental and Molecular Dynamics Simulation Data. *Appl. Surf. Sci.* **2020**, *506*, 144914.
(41) Zhao, X.; Bhagia, S.; Gomez-Maldonado, D.; Tang, X.; Wasti, S.; Lu, S.; Zhang, S.; Parit, M.; Rencheck, M. L.; Korey, M.; Jiang, H. Bioinspired Design Toward Nanocellulose-Based Materials. *Mater. Today* **2023**, *66*, 409−430.
(42) Munch, E.; Launey, M. E.; Alsem, D. H.; Saiz, E.; Tomsia, A. P.; Ritchie, R. O. Tough, Bio-Inspired Hybrid Materials. *Science* **2008**, *322* (5907), 1516−1520.
(43) Wegst, U. G.; Bai, H.; Saiz, E.; Tomsia, A. P.; Ritchie, R. O. Bioinspired Structural Materials. *Nat. Mater.* **2015**, *14* (1), 23−36.
(44) Soltan, D.; Ranade, R.; Li, V. A Bio-Inspired Cementitious Composite for High Energy Absorption in Infrastructural Applications. *Blucher Mater Sci. Proc.* **2014**, *1* (1), 1−4.
(45) Mei, Y.; Liu, J.; Cui, Y.; Li, F.; Tang, X.; Sun, M.; Chi, R.; Zhang, Y.; Zhang, A.; Chen, K. Mechanically Excellent Nacre-Inspired Protective Steel-Concrete Composite Against Hypervelocity Impacts. *Sci. Rep.* **2021**, *11* (1), 21930.
(46) Harmal, A.; Khouchani, O.; El-Korchi, T.; Tao, M.; Walker, H. W. Bioinspired Brick-and-Mortar Geopolymer Composites with Ultra-High Toughness. *J. Cem. Concr. Compos.* **2023**, *137*, 104944.
(47) Rosewitz, J. A.; Choshali, H. A.; Rahbar, N. Bioinspired Design of Architected Cement-Polymer Composites. *J. Cem. Concr. Compos.* **2019**, *96*, 252−265.
(48) Restrepo, V.; Martinez, R. V. Bioinspired Cabrication of Reconfigurable Elastomeric Cementitious Structures Using Self-Healing Mechanical Adhesives Interfaces. *Mater. Design.* **2021**, *205*, 109691.
(49) Soltan, D. G.; Li, V. C. Nacre-Inspired Composite Design Approaches for Large-Scale Cementitious Members and Structures. *J. Cem. Concr. Compos.* **2018**, *88*, 172−186.
(50) Pan, H.; She, W.; Zuo, W.; Zhou, Y.; Huang, J.; Zhang, Z.; Geng, Z.; Yao, Y.; Zhang, W.; Zheng, L.; et al. Hierarchical Toughening of A Biomimetic Bulk Cement Composite. *ACS Appl. Mater. Interfaces* **2020**, *12* (47), 53297−53309.
(51) Pan, H.; Geng, Z.; Huang, P.; Zhou, Y.; Tang, J.; She, W.; Liu, J. A Bionic Solution to Make Cement Matrix Tough. *J. Cem. Concr. Compos.* **2023**, *136*, 104881.
(52) Wang, F.; Du, Y.; Jiao, D.; Zhang, J.; Zhang, Y.; Liu, Z.; Zhang, Z. Wood-Inspired Cement with High Strength and Multifunctionality. *Adv. Sci.* **2021**, *8* (3), 2000096.
(53) Chen, Y.; Zheng, Y.; Zhou, Y.; Zhang, W.; Li, W.; She, W.; Liu, J.; Miao, C. Multi-Layered Cement-Hydrogel Composite with High Toughness, Low Thermal Conductivity, and Self-healing capability. *Nat. Commun* **2023**, *14* (1), 3438.
(54) Liu, X.; Feng, P.; Agudo, C. R.; Sun, H.; Yu, X.; Avaro, J.; Huang, J.; Hou, D.; Ran, Q.; Hong, J.; et al. High Energy Absorption Nacre-Like Calcium Silicate Hydrate (C-S-H) Composite Toward Elastic Cementitious Materials. *Adv. Funct. Mater.* **2024**, *34* (7), 2307437.
(55) Wang, Y.; Goodman, S.; Bao, Y.; Meng, W. Morphological, Microstructural, and Mechanical Properties of Highly-Ordered C−S−H Regulated by Cellulose Nanocrystals (CNCs). *J. Cem. Concr. Compos.* **2023**, *143*, 105276.
(56) Starr, J.; Soliman, E. M.; Matteo, E. N.; Dewers, T.; Stormont, J. C.; Taha, M. M. R. Mechanical Characterization of Low Modulus Polymer-Modified Calcium-Silicate-Hydrate (C−S−H) Binder. *J. Cem. Concr. Compos.* **2021**, *124*, 104219.
(57) Chen, Y.; Fu, J.; Dang, B.; Sun, Q.; Li, H.; Zhai, T. Artificial Wooden Nacre: A High Specific Strength Engineering Material. *ACS Nano* **2020**, *14* (2), 2036−2043.
(58) Li, M.; Wang, M.; Zhao, N.; Bai, H. Scalable Fabrication of High-Performance Bulk Nacre-Mimetic Materials on A Nanogrooved Surface. *ACS Nano* **2022**, *16* (9), 14737−14744.
(59) Han, J.; Du, G.; Gao, W.; Bai, H. An Anisotropically High Thermal Conductive Boron Nitride/Epoxy Composite Based on Nacre-Mimetic 3D Network. *Adv. Funct. Mater.* **2019**, *29* (13), 1900412.
(60) Delhorme, M.; Labbez, C.; Turesson, M.; Lesniewska, E.; Woodward, C. E.; Jonsson, B. Aggregation of Calcium Silicate Hydrate Nanoplatelets. *Langmuir* **2016**, *32* (8), 2058−2066.
(61) Clogston, J. D.; Patri, A. K. Zeta Potential Measurement. In *Characterization of Nanoparticles Intended for Drug Delivery*; Springer: 2011; pp. 6370.
(62) Picker, A.; Nicoleau, L.; Nonat, A.; Labbez, C.; Cölfen, H. Influence of Polymers on the Nucleation of Calcium Silicate Hydrates. *Cem. Concr. Res.* **2023**, *174*, 107329.
(63) Song, S.; Qiang, S.; Liang, J.; Li, L.; Shi, Y.; Nie, J.; Chen, T.; Yao, S.; Zhang, M. Cellulose Nanofibril/Mineral Composites Induced by H-bond/Ionic Coordination in Co-Refining System. *Carbohydr. Polym.* **2022**, *289*, 119425.
(64) Morita, M.; Matsumura, F.; Shikata, T.; Ogawa, Y.; Kondo, N.; Shiraga, K. Hydrogen-Bond Configurations of Hydration Water Around Glycerol Investigated by HOH Bending and OH Stretching Analysis. *J. Phys. Chem. B* **2022**, *126* (47), 9871−9880.
(65) Zhao, N.; Yang, M.; Zhao, Q.; Gao, W.; Xie, T.; Bai, H. Superstretchable Nacre-Mimetic Graphene/Poly (vinyl alcohol) Composite Film Based on Interfacial Architectural Engineering. *ACS Nano* **2017**, *11* (5), 4777−4784.
(66) Wan, H.; Leung, N.; Algharaibeh, S.; Sui, T.; Liu, Q.; Peng, H.-X.; Su, B. Cost-Effective Fabrication of Bio-Inspired Nacre-Like Composite Materials with High Srength and Toughness. *Compos., Part B* **2020**, *202*, 108414.
(67) Sun, J.; Bhushan, B. Hierarchical Structure and Mechanical Properties of Nacre: A Review. *RSC Adv.* **2012**, *2* (20), 7617−7632.
(68) Karkar, Z.; Guyomard, D.; Roué, L.; Lestriez, B. A Comparative Study of Polyacrylic Acid (PAA) and Carboxymethyl Cellulose (CMC) Binders for Si-Based Electrodes. *Electrochim. Acta* **2017**, *258*, 453−466.
(69) Clegg, W.; Kendall, K.; Alford, N. M.; Button, T.; Birchall, J. A Simple Way to Make Tough Ceramics. *Nature* **1990**, *347* (6292), 455−457.
(70) Tabatabaei, M.; Taleghani, A. D.; Alem, N. Nanoengineering of Cement Using Graphite Platelets to Refine Inherent Microstructural Defects. *Compos., Part B* **2020**, *202*, 108277.
(71) Morits, M.; Verho, T.; Sorvari, J.; Liljeström, V.; Kostiainen, M. A.; Gröschel, A. H.; Ikkala, O. Toughness and Fracture Properties in Nacre-Mimetic Clay/Polymer Nanocomposites. *Adv. Funct. Mater.* **2017**, *27* (10), 1605378.
(72) Jain, J.; Neithalath, N. Analysis of Calcium Leaching Behavior of Plain and Modified Cement Pastes in Pure Water. *Cem. Concr. Compos.* **2009**, *31* (3), 176−185.
(73) Liu, Q.-F.; Shen, X.-H.; Šavija, B.; Meng, Z.; Tsang, D. C.; Sepasgozar, S.; Schlangen, E. Numerical Study of Interactive Ingress of Calcium Leaching, Chloride Transport and Multi-Ions Coupling in Concrete. *Cem. Concr. Res.* **2023**, *165*, 107072.
(74) Li, H.; Liu, Y.; Yang, K.; Liu, C.; Guan, X.; Liu, S.; Jing, G. Effects of Synthetic CSH-Tartaric Acid Nanocomposites on the Properties of Ordinary Portland Cement. *Cem. Concr. Compos.* **2022**, *129*, 104466.
(75) Du, F.; Zhu, W.; Yang, R.; Zhang, Y.; Wang, J.; Li, W.; Zuo, W.; Zhang, L.; Chen, L.; She, W.; et al. Bioinspired Super Thermal Insulating, Strong and Low Carbon Cement Aerogel for Building Envelope. *Adv. Sci.* **2023**, *10* (18), 2370115.
(76) Nicoleau, L.; Gädt, T.; Chitu, L.; Maier, G.; Paris, O. Oriented Aggregation of Calcium Silicate Hydrate Platelets by the Use of Comb-Like Copolymers. *Soft Matter* **2013**, *9* (19), 4864−4874.
(77) Kanchanason, V.; Plank, J. Role of pH on the Structure, Composition and Morphology of CSH−PCE Nanocomposites and

https://doi.org/10.1021/acsnano.4c08200
ACS Nano 2024, 18, 23655−23671

Their Effect on Early Strength Development of Portland Cement. *Cem. Concr. Res.* **2017**, *102*, 90−98.
(78) Avella, M.; Errico, M. E.; Martuscelli, E. Novel PMMA/$CaCO_3$ Nanocomposites Abrasion Resistant Prepared by An *in situ* Polymerization Process. *Nano Lett.* **2001**, *1* (4), 213−217.
(79) Ali, U.; Karim, K. J. B. A.; Buang, N. A. A Review of the Properties and Applications of Poly (methyl methacrylate)(PMMA). *Polym. Rev.* **2015**, *55* (4), 678−705.
(80) Mark, J. E. *Physical Properties of Polymers Handbook*; Springer: 2007, Vol. *1076*.
(81) Zhao, H.; Yue, Y.; Guo, L.; Wu, J.; Zhang, Y.; Li, X.; Mao, S.; Han, X. Cloning Nacre's 3D Interlocking Skeleton in Engineering Composites to Achieve Exceptional Mechanical Properties. *Adv. Mater.* **2016**, *28* (25), 5099−5105.

https://doi.org/10.1021/acsnano.4c08200
ACS Nano 2024, 18, 23655−23671